

UNIVERSITY OF COPENHAGEN



---

# Exploring the properties of complex oxide interfaces patterned by optical lithography

## **Bachelor thesis**

Ricci Erlandsen

Nanoscience

Supervisor: Thomas Sand Jespersen

Submitted on: 14-06-2017

# Exploring the properties of complex oxide interfaces patterned by optical lithography

Ricci Erlandsen<sup>1\*</sup>

<sup>1</sup>*Center for Quantum Devices and Nano-Science Center, Niels Bohr Institute, University of Copenhagen, Universitetsparken 5, DK-2100 Copenhagen, Denmark*

Rasmus Tindal Dahm<sup>1</sup>, Merlin von Soosten<sup>1,2</sup>, Anders Valdemar Bjørlig<sup>1</sup>, Yulin Gan<sup>2</sup>, Wei Niu<sup>2</sup>, Yu Zhang<sup>2</sup>, Dennis Christensen<sup>2</sup>, Nini Pryds<sup>2</sup>, Yunzhong Chen<sup>2</sup> and Thomas Sand Jespersen<sup>1</sup>

<sup>2</sup>*Department of Energy Conversion and Storage, Technical University of Denmark, Risø Campus, DK-4000 Roskilde, Denmark*

(Dated: June 14, 2017)

This study revolves around the patterning of interfaces based on SrTiO<sub>3</sub>/LaAlO<sub>3</sub> heterostructures by using optical lithography. Limitations of optical lithography were determined by room temperature measurements. Low temperature measurements were carried out to explore the properties of devices patterned with this method. Domain structure effects are probed by devices of different orientations, however results showed no clear sign of such effects. The sheet resistance is expressed as a function of temperature, depending upon electron-phonon scattering and impurity scattering. Hall effect measurements revealed a magnetic field dependency for  $\rho_{xx}$  as explained by the two-band model accounting for an extra charge carrier. Carrier densities were of expected values, however with considerably lower mobilities. A backgate sweep enhanced the minimum in  $\rho_{xx}$  at zero magnetic field, indicating effects resembling weak anti-localization that were present even after the gate was turned off.

## I. INTRODUCTION

The modern world demands continual advancement in fields such as electronics. Optimization is a key factor in perfecting electronic devices. Complex oxides exhibits exceptional properties such as gate-tunable superconductivity[1] and ferromagnetism[2], that could result modern electronic devices based on oxides[3, 4]. A particularly interesting phenomena is the formation of a two dimensional electron gas (2DEG) between the two insulating oxides, SrTiO<sub>3</sub> (STO) and LaAlO<sub>3</sub> (LAO)[5], at a critical thickness (3 unit cells) of LAO[6, 7]. LaSrMnO<sub>3</sub> (LSM) is traditionally used as a hard mask to define the insulating STO/LSM/LAO regions[8, 9] along with electron beam for patterning[8]. The focus of this study is patterning with optical lithography by using the LED-writer along with photoresist. The interest is in the properties of samples patterned by this method. Three samples S1, S2, S3 are fabricated to test the limitations of optical lithography. Domain structure effects as reported in other studies[10, 11] are probed by rotating patterned devices to possibly find a relation between orientation and conductance. All samples are STO/LAO but with varying hard masks and orientations of the crystal plane. S1 is a (001)-oriented sample with photoresist as a hard mask. S2 is a (001)-oriented sample with LSM as a hard mask and is viewed as the conventional sample. S3 is a (111)-oriented sample with LSM. Low temperature and room temperature (RT) measurements are performed on S1 to investigate if photoresist is a suitable hard mask.

## II. FABRICATION

$5 \times 5 \times 0.5$  mm<sup>3</sup> STO substrates were chemically and thermally treated according to the recipe described in appendix A. The substrate treatment is performed to achieve TiO<sub>2</sub>-terminated STO substrates[12]. Amorphous LSM (a-LSM) was deposited using pulsed laser deposition (PLD) (figure 1b). The deposition was carried out at RT and at ultra high vacuum. The patterning was achieved by using a photoresist (AZ1505) and the Heidelberg  $\mu$ PG 501 Maskless Aligner (LED-writer) with an exposure time of 16 ms. It has been proved in previous studies that the interface is not damaged by using optical lithography[13]. The exposed sample was then developed for 1 minute in MF321-developer followed by 1 minute in milli-Q water (figure 1c). Selective wet etching was used (KI/HCl etch) to reach the surface of STO (figure 1d). The samples were etched for 30s which has been determined the best etch time as described in appendix C. The residual resist was then removed by immersing in NMP for 5 minutes at 80°C followed by surface cleaning with acetone and IPA (figure 1e). The samples were then plasma-ashed for 2 minutes to remove residual resist and other organic material. A protocol for exposure, development and etching is found in appendix C. Figure 2a-d shows how the exposure, development and etching turns out. It shows great consistency with minimal over-etching and over-exposure. Atomic force microscopy (AFM) is used to verify that the STO surface is reached. 12 nm amorphous LAO (a-LAO) was then deposited by PLD to achieve the conducting a-LAO/STO interface or insulating a-LAO/a-LSM/STO heterostructures (figure 1f). The resist is not capable of handling high temperatures, hence the deposition of a-LAO at RT. The samples were then glued (conductive silver paste) to a sample

---

\* lnk170@alumni.ku.dk

holder that is marked with Au-contacts where the sample was bonded using Al-wire with the FS auto-bonder by ultrasound. RT measurements were performed to ensure conducting samples. The low temperatures were achieved by the Oxford He cryostat.

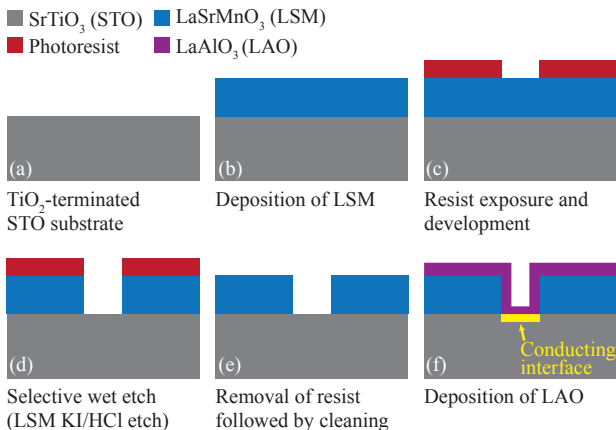


FIG. 1. Schematic view of the fabrication process. (a) A  $\text{TiO}_2$ -terminated STO substrate. (b) LSM is deposited using PLD. (c) The resist pattern is obtained using an LED-writer and photoresist. (d) Selective wet etching (KI/HCL etch) is utilized to ensure the STO surface is reached. (e) The residual resist is then removed followed by surface cleaning. (f) LAO is deposited using PLD resulting in conducting STO/LAO interfaces or insulating STO/LSM/LAO heterostructures.

### III. RESULTS AND DISCUSSION

Figure 2e shows the data for the RT measurements. The solid lines represents the resistance as a function of channel thickness, showing a  $R \propto \frac{1}{W}$  tendency, where  $W$  is the channel thickness. The resist sample (S1 - blue line) and sample S2 (red line) exhibit almost identical behavior, where the (111)-oriented sample (S3 - green line) shows much larger resistances. S2 is the only sample to not conduct at  $W = 2 \mu\text{m}$ , which is explained in appendix E. The dots denotes the leakage current. All three samples leak with a spacing,  $d = 1 \mu\text{m}$ , where the measured resistance at leakage for S1 is 10 times larger. Only S3 leaks at  $d = 2 \mu\text{m}$ . It seems the resist sample S1 reigns supreme in terms of leakage current and conductivity, which makes it valuable for low temperature measurements. All data in this study are measured using the 4-point probe method, neglecting the contact resistances, however when the probes were switched around (e.g. source and voltage probe A) a slight change in resistance were measured, indicating that the values are not absolute. The limitations of the patterning process involving the LED-writer is determined by the RT measurements. A channel thickness limit  $W \geq 1 \mu\text{m}$  and spacing limit  $d \geq 2 \mu\text{m}$  is extracted from figure 2e, however S3 leaks at  $d = 2 \mu\text{m}$ , suggesting that a (111)-oriented sample is

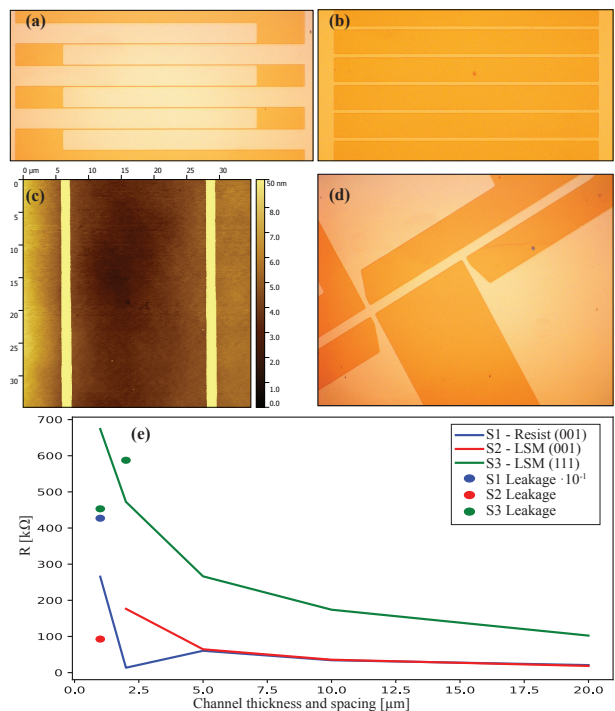


FIG. 2. Etched sample (S2), with RT measurements for all three samples. (a) Optical image of etched design for testing the leakage current. The spacing between channels is  $2 \mu\text{m}$ . (b) Optical image of etched design for measuring the resistance as a function of channel thickness. The thickness is  $2 \mu\text{m}$  for this device. (c) AFM image of the three lower channels in (a), showing well-defined separation of neighboring channels. (d) Optical image of an etched hall bar with a channel thickness of  $10 \mu\text{m}$  and three voltage probes. The narrow region connecting channel and probe is  $5 \mu\text{m}$ . (e) Plot showing all of the RT measurements. Solid lines represent the resistance as a function of channel thickness. Dots represent leakage current as a function of spacing between channels.

either different from (001)-oriented samples or is inaccurate due to experimental errors.

Two series consisting of six hall bars with a channel thickness of  $30 \mu\text{m}$  and  $10 \mu\text{m}$ , both with varying orientations were designed to test for domain structure effects. The hall bars vary from  $\theta = 0^\circ$  to  $\theta = 150^\circ$  in steps of  $30^\circ$ . The hall bars with a channel width of  $10 \mu\text{m}$  are shown in figure 3 with AFM images of the terrace structure of each hall bar, however the series of  $30 \mu\text{m}$  thick hall bars were chosen for measurements to ensure conductivity. The terraces show admirable consistency throughout the sample surface. The measurements show no clear relation between conductance and orientation (figure 15 in H), which is likely a result of small domains compared to the thickness of the hall bars ( $30 \mu\text{m}$ ), hence the  $10 \mu\text{m}$  thin hall bars. Hall bar 5 ( $\theta = 120^\circ$ ) stands out in almost all measurements with  $\sim 4$  times larger resistance values, which contradicts the locally enhanced conductance effect caused by the domain structure, thus the inaccuracy of hall bar 5 is likely due to experimental errors.

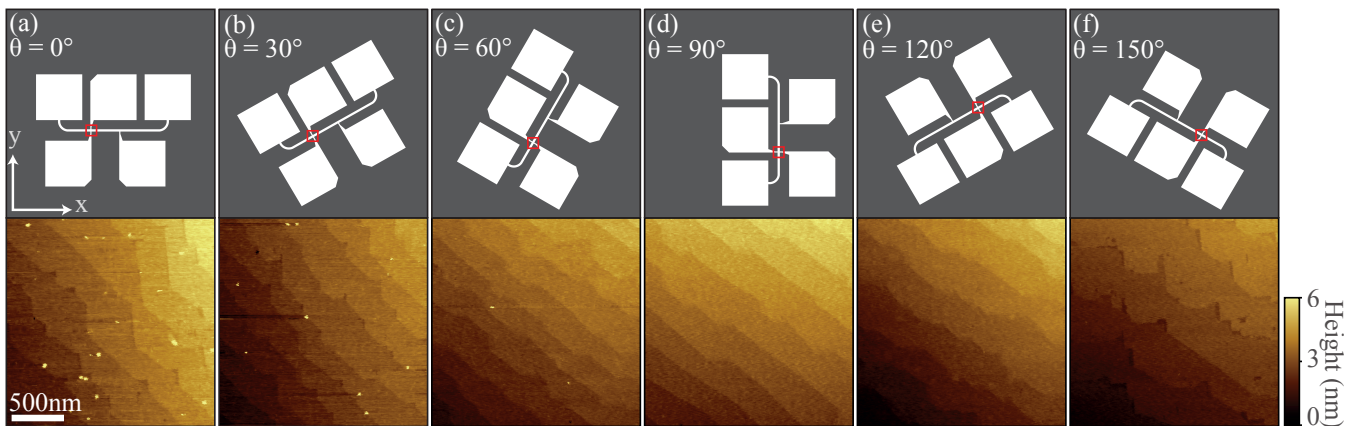


FIG. 3. Schematic view of six hall bars with varying orientations ( $\theta$ ) and corresponding AFM images matching the red squares. The width of the hall bar channel is  $10 \mu\text{m}$ . Scale bar depicts  $500\text{nm}$  for all AFM images. The  $xy$ -coordinates are to clarify that the hall bars are rotating. (a) hall bar with orientation  $\theta = 0^\circ$  with corresponding AFM image taken between the two transverse voltage probes as marked by the red square. (b)-(f) Same as (a), however with  $\theta$  increasing in steps of  $30^\circ$  from  $0^\circ$  in (a) to  $150^\circ$  in (f). All AFM images exhibit the same terrace structure with approximately the same slope, thus suggesting the sample is uniform and the terrace structure is consistent throughout the sample surface.

S1 was the only sample to be loaded into the cryostat due to time constraints. Figure 4a shows the cool-down data ( $R_{xx}$  vs.  $T$ ) for sample S1. As the temperature is lowered it is expected for a 2DEG, that the mobility will increase due to less electron-phonon scattering[14]. This results in an increasing conductance during cool-down. The main contributor to conductance in this system is oxygen vacancies[9], which has been observed by utilizing devices consisting of nanostructures, indicating that the oxygen vacancies gather in conductive filaments at low temperatures[15]. In the temperature range  $100 \text{ K} < T < 300 \text{ K}$  the resistance is expected to be dominated by electron-phonon scattering ( $R_{el-ph}$ ), where  $R_{el-ph} \propto T^2$ [16]. In the range  $10 \text{ K} < T < 100 \text{ K}$ , the sheet resistance is expected to be  $R_s = R_{el-ph} + R_{imp}$ , where  $R_{imp}$  is the impurity scattering caused by oxygen vacancies, which is described in a previous study by Fuchs et al.[17]. They also find a model expressing  $R_s(T)$ :

$$R_s = A \left[ 1 - \exp\left(-\frac{T_a}{T}\right) \right] \left[ \frac{T_1}{2} \coth\left(\frac{T_1}{2T}\right) - T_0 \right]^2 + B \times T^2 \quad (1)$$

The exponential term describes the number of charged impurities ( $N_i$ ). The second term describes the efficiency of the impurities and is derived from the dielectric permittivity of STO,  $\epsilon(T)$ , which is defined by the Barrett formula[18]:

$$\epsilon(T) = C (T_1/2 \times \coth(T_1/2T) - T_0)^{-1} \quad (2)$$

where  $T_1$  is the temperature where quantum effects become important as described by Barrett[18],  $T_0$  the critical temperature from classical mean-field theory[17, 19] and  $C$  is the Curie constant. By using the impurity potential  $V \propto \epsilon^{-1}$  and Fermi's golden rule,  $R_{imp} \propto N_i \times V^2$ ,

it is possible to understand the temperature dependence of the impurity scattering, due to the number of charged impurities given as  $N_i(T)$ . The values for  $T_1$ ,  $T_a$ ,  $T_0$ ,  $B$  and  $A$  are adapted from the fitting model at ambient pressure from Fuchs et al.[17]. The model is in excellent agreement with the data in figure 4a, leading to a better interpretation of the cool-down process. The model is plotted in appendix I, showing exceptional comparability to the cool-down data. The model was not included in figure 4a due to time constraints. From equation (1) it is clear that  $R_s$  decreases at lower temperatures due to a larger number of charged impurities and a larger dielectric constant[7]. It starts increasing again around temperatures of  $\sim 10\text{K}$ , which could be explained by the Kondo effect, which is discussed in this system along with the polar discontinuity contributing to the interface conductivity by Brinkman et al.[2].

Hall effect measurements were performed for all six hall bars with a channel width of  $30 \mu\text{m}$  and varying orientations. Two hall bars (number 1 and 4, where  $\theta = 0^\circ$  and  $\theta = 150^\circ$ , respectively) were selected for a more thorough study. The hall measurements for these are plotted in figure 4b-c leading to the extraction of carrier density  $n_s = -1/(eR_{xy})$  and mobility  $\mu = (en_s R_{xx})^{-1}$ , where  $e$  is the elementary charge. The values are determined by using the slope of figure 4c from 1 to 5 T. The blue curves represent hall bar 1 (HB1), while the red curves represent hall bar 4 (HB4) which is clarified in appendix B. The carrier density is found to be  $n_s = 2.07 \times 10^{13} \text{ cm}^{-2}$  and the mobility,  $\mu = 659.73 \text{ cm}^2/\text{Vs}$  for HB1. The values for HB4 are  $n_s = 2.12 \times 10^{13} \text{ cm}^{-2}$  and  $\mu = 549.73 \text{ cm}^2/\text{Vs}$ . The carrier densities are in good agreement with other studies, however the mobility seems to be much lower than usual for both hall bars[8]. This sample uses photoresist as a hard mask, which could explain the

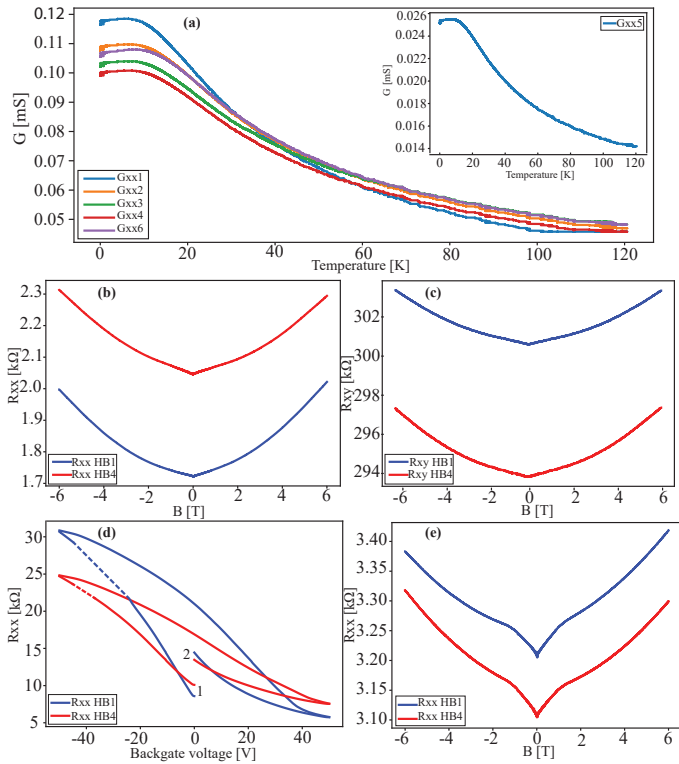


FIG. 4. Data for low temperature measurements. (a) Cool-down plot showing conductance as a function of temperature. Inset: conductance for hall bar 5 ( $G_{xx5}$ ) which is  $\sim 4$  times lower than the rest. (b) Longitudinal resistance ( $R_{xx}$ ) versus magnetic field from the hall measurement showing hall bar 1 (blue curve) and hall bar 4 (red curve). (c) Transverse resistance ( $R_{xy}$ ) versus magnetic field. (d) Backgate swept from 0V to -50V, then to 50V, then back to 0V again. The dashed lines are to guide the eye, as the system overloaded in this interval. The numbers 1 and 2 designates start and end of the sweeping, respectively. (e) Same as (b), however performed after the gate-sweeping.

low mobility compared to samples with LSM as the hard mask.  $R_{xx}$  deviates from an ordinary hall characterization. In figure 4b it is clear that  $R_{xx}$  has an obvious B-dependency. The nonlinearity in  $R_{xy}$  (figure 4c) is also different from textbook hall measurements. It seems that a 2-band model accounting for two different carrier types is necessary to explain the nonlinear plots. Kane et al.[20] explains this by using equations describing the B-dependency for  $R_{xx}$  in low magnetic field:

$$\rho_{xx} = \frac{1}{e(n_1\mu_1 + n_2\mu_2)} \quad (3)$$

For high magnetic field:

$$\rho_{xx} = \frac{(n_1/\mu_1) + (n_2/\mu_2)}{e(n_1 + n_2)^2} \quad (4)$$

This explains the nonlinear hall effect measurements, where it is clear that another band is contributing to the

conductance, thus the extra set of values for  $n_s$  and  $\mu$  due to having another charge carrier. A backgate sweep was performed as plotted in figure 4d. The backgate voltage starts at 0V and is swept to -50V, then swept to 50V, then back to 0V. As seen in the sweeping plot, the longitudinal resistance for both hall bars increases. This could be investigated further, by sweeping back and forth between -50V and 50V and perhaps for an even higher range. The backgate is turned off and a new hall measurement is then performed on the same two hall bars and  $R_{xx}$  for both hall bars are plotted in figure 4e. The carrier density and mobility values are extracted once again,  $n_s = 2.44 \times 10^{13} \text{ cm}^{-2}$  and  $\mu = 309.87 \text{ cm}^2/\text{Vs}$  for HB1, while the values for HB4 are  $n_s = 3.50 \times 10^{13} \text{ cm}^{-2}$  and  $\mu = 221.04 \text{ cm}^2/\text{Vs}$ . Comparing these values (before and after gate sweeping) and looking at the equation for conductivity[21],  $\sigma = e\mu n_s$  it is possible to explain why the curves for HB1 and HB4 swap places from figure 4b to 4e. It is clear that the overall conductivity decreases after sweeping the backgate, however the peak in conductance at  $B=0$  T becomes sharper. The interesting feature at zero magnetic field (a maximum in conductance) could be related to weak anti-localization (WAL) as observed in a study by Cavaglia et al.[22]. They observe the same sharp increase in the zero field peak, however with a fixed backgate voltage. Cavaglia et al. state that an applied electrical field leads to a change in the spin-coherence resulting in a stronger spin-orbit coupling which counteracts weak localization, thus giving rise to WAL. The sample in this study is affected by the backgate even after the gate has been turned off. The sharp decrease in resistance around  $B=0$  T is not as explicit in 4b as it is in figure 4e, which is the exact same hall bars before and after the gate-sweeping, respectively. It is therefore plausible that weak anti-localization effects are enhanced, due to a larger spin-orbit coupling by gate-sweeping this 2DEG, however this could also be explained by the two-band model, if the carrier density and mobility have been affected by the gate.

#### IV. CONCLUSIONS

In conclusion, this study determined the limitations of optical lithography. A channel thickness limit,  $W \geq 1 \mu\text{m}$  and a limit of the spacing between two neighboring channels,  $d \geq 2 \mu\text{m}$  was determined from the room temperature measurements. A clear relation between device orientation and conductance was not observed, indicating that domain structure effects were not present in this study, thus signifying the consistency throughout the sample surface as imaged with AFM. Low temperature data display great comparability to a fitting model described in a previous study, accounting for both electron-phonon scattering and impurity scattering. A two-band model was presented to explain the nonlinear hall effect measurements, indicating that this is not an ordinary 2DEG. Effects resembling Weak anti-localization were

found to be enhanced by sweeping a backgate from -50V to 50V and the effects seems to be permanent since the sample is affected even after the gate has been turned off, however the effects could possibly be induced by changes in the carrier density and mobility as described by the two-band model. This study proves that it is possible to use photoresist as a hard mask in the patterning process of SrTiO<sub>3</sub>/LaAlO<sub>3</sub> heterostructures. Further studies could include low temperature measurements on the samples utilizing LSM and other types of resists e.g. e-beam resist. The thin hall bars could be probed in the cryostat

for a more thorough study of domain structure effects.

## ACKNOWLEDGEMENTS

Thanks to Yunzhong Chen and all the people at DTU for helping out with the fabrication process and for fruitful discussions. Thanks to Merlin von Soosten for helping with all of the measurements including the experimental setups. A big thanks to Thomas Sand Jespersen for guidance and clarification along the way.

- 
- [1] Nicolas Reyren, S Thiel, AD Caviglia, L Fitting Kourkoutis, G Hammerl, C Richter, CW Schneider, T Kopp, A-S Rüetschi, Didier Jaccard, et al. Superconducting interfaces between insulating oxides. *Science*, 317(5842):1196–1199, 2007.
- [2] Alexander Brinkman, M Huijben, M Van Zalk, J Huijben, U Zeitler, JC Maan, WG Van der Wiel, G Rijnders, DHA Blank, and H Hilgenkamp. Magnetic effects at the interface between non-magnetic oxides. *Nature materials*, 6(7):493–496, 2007.
- [3] Stefan Thiel, German Hammerl, A Schmehl, CW Schneider, and Jochen Mannhart. Tunable quasi-two-dimensional electron gases in oxide heterostructures. *Science*, 313(5795):1942–1945, 2006.
- [4] Darrell G Schlom and Jochen Mannhart. Oxide electronics: interface takes charge over si. *Nature materials*, 10:168–169, 2011.
- [5] A. Ohtomo and H.Y. Hwang. A high-mobility electron gas at the LaAlO<sub>3</sub>/SrTiO<sub>3</sub> heterointerface. *Nature*, 427(6973):423–426, 2004.
- [6] Cheng Cen, Stefan Thiel, Jochen Mannhart, and Jeremy Levy. Oxide nanoelectronics on demand. *Science*, 323(5917):1026–1030, 2009.
- [7] Joseph A Sulpizio, Shahal Ilani, Patrick Irvin, and Jeremy Levy. Nanoscale phenomena in oxide heterostructures. *Annual Review of Materials Research*, 44:117–149, 2014.
- [8] Felix Trier, Guenevere EDK Prawiroatmodjo, Merlin von Soosten, Dennis Valbjørn Christensen, Thomas Sand Jespersen, YZ Chen, and Nini Pryds. Patterning of high mobility electron gases at complex oxide interfaces. *Applied Physics Letters*, 107(19):191604, 2015.
- [9] Yunzhong Chen, Nini Pryds, José E Kleibeuker, Gertjan Koster, Jirong Sun, Eugen Stamate, Baogen Shen, Guus Rijnders, and Søren Linderoth. Metallic and insulating interfaces of amorphous srtio3-based oxide heterostructures. *Nano letters*, 11(9):3774–3778, 2011.
- [10] Beena Kalisky, Eric M Spanton, Hilary Noad, John R Kirtley, Katja C Nowack, Christopher Bell, Hiroki K Sato, Masayuki Hosoda, Yanwu Xie, Yasuyuki Hikita, et al. Locally enhanced conductivity due to the tetragonal domain structure in LaAlO<sub>3</sub>/SrTiO<sub>3</sub> heterointerfaces. *Nature materials*, 12(12):1091–1095, 2013.
- [11] Maayan Honig, Joseph A Sulpizio, Jonathan Drori, Arjun Joshua, Eli Zeldov, and Shahal Ilani. Local electrostatic imaging of striped domain order in LaAlO<sub>3</sub>/SrTiO<sub>3</sub>. *Nature materials*, 12(12):1112–1118, 2013.
- [12] Gertjan Koster, Boike L Kropman, Guus JHM Rijnders, Dave HA Blank, and Horst Rogalla. Quasi-ideal strontium titanate crystal surfaces through formation of strontium hydroxide. *Applied Physics Letters*, 73(20):2920–2922, 1998.
- [13] Christof W Schneider, S Thiel, G Hammerl, Christoph Richter, and J Mannhart. Microlithography of electron gases formed at interfaces in oxide heterostructures. *Applied physics letters*, 89(12):122101, 2006.
- [14] Y. Q. Tao, D. J. Chen, Y. C. Kong, B. Shen, Z. L. Xie, P. Han, R. Zhang, and Y. D. Zheng. High-temperature transport properties of 2deg in AlGa<sub>N</sub>/Ga<sub>N</sub> heterostructures. *Journal of Electronic Materials*, 35(4):722–725, 2006.
- [15] M. Z. Minhas, A. Miller, F. Heyroth, H. H. Blaschek, and G. Schmidt. Temperature dependent giant resistance anomaly in LaAlO<sub>3</sub>/SrTiO<sub>3</sub> nanostructures. *ArXiv e-prints*, October 2016.
- [16] Dirk Van Der Marel, Jacobus Lodevicus Martinu van Mechelen, and II Mazin. Common fermi-liquid origin of t 2 resistivity and superconductivity in n-type sr tio 3. *Physical Review B*, 84(20):205111, 2011.
- [17] D Fuchs, A Sleem, R Schäfer, AG Zaitsev, M Meffert, D Gerthsen, R Schneider, and H v Löhneysen. Incipient localization of charge carriers in the two-dimensional electron system in LaAlO<sub>3</sub>/SrTiO<sub>3</sub> under hydrostatic pressure. *Physical Review B*, 92(15):155313, 2015.
- [18] John H Barrett. Dielectric constant in perovskite type crystals. *Physical Review*, 86(1):118, 1952.
- [19] Ruiping Wang, Norihiko Sakamoto, and Mitsuru Itoh. Effects of pressure on the dielectric properties of SrTi<sub>18</sub>O<sub>3</sub> and SrTi<sub>16</sub>O<sub>3</sub> single crystals. *Physical Review B*, 62(6):R3577, 2000.
- [20] M J Kane, N Apsley, D A Anderson, L L Taylor, and T Kerr. Parallel conduction in GaAs/Al<sub>x</sub>Ga<sub>1-x</sub>As modulation doped heterojunctions. *Journal of Physics C: Solid State Physics*, 18(29):5629, 1985.
- [21] Gervasi Herranz, Mario Basletić, Manuel Bibes, C Carrétéro, Emil Tafra, E Jacquet, Karim Bouzehouane, C Deranlot, Amir Hamzić, J-M Broto, et al. High mobility in LaAlO<sub>3</sub>/SrTiO<sub>3</sub> heterostructures: origin, dimensionality, and perspectives. *Physical review letters*, 98(21):216803, 2007.
- [22] AD Caviglia, M Gabay, Stefano Gariglio, Nicolas Reyren, Claudia Cancellieri, and J-M Triscone. Tunable rashba spin-orbit interaction at oxide interfaces. *Physical review letters*, 104(12):126803, 2010.

## Appendix A: Substrate treatment

This recipe is developed by Dennis V. Christensen, Felix Trier and Yunzhong Chen.

### Chemical treatment

1. **Preheat water** in an ultrasonic bath to  $70^{\circ}\text{C}$  (7/8 filled)
2. **Immerse substrate in EtOH** and sonicate for 5 min. at RT followed by drying and defect/dirt inspection
3. **Repeat step 2 with acetone.**
4. **Immerse substrate in milli-Q water** (or de-ionized-water) and sonicate for 20 min. at  $70^{\circ}\text{C}$  followed by drying and defect/dirt inspection.
5. Prepare an 3 : 1 : 16  $\text{HCl}(37\%) : \text{HNO}_3(66\%) : \text{H}_2\text{O}(\text{milli} - \text{Q})$  acid solution (e.g. 9ml:3ml:48ml for a total of 60ml) by adding HCl slowly to  $\text{HNO}_3$  (and not visa versa). Let it be for 5 min. **Immerse substrate in acid solution** and ultrasonicate for 20 min. at  $70^{\circ}\text{C}$  and transfer directly to water (step 6). Clean alumina oven boxes with the acid solution.
6. **Immerse substrate in milli-Q water** (or de-ionized water) and sonicate for 30 s. at RT followed by drying and defect/dirt inspection.

### Annealing in tube furnace

1. **Place** tube in furnace with  $\approx 13\text{cm}$  of each tube-end outside the furnace. Check the thermocouple with corresponding plug in rear end reaches 50 cm into the tube.
2. **Place** substrate in alumina boxes and insert the box close to thermocouple **in the center of the furnace**. Set the flow rate of oxygen through the tube to  $\approx 10$  (arbitrary units) with 5-10 bubbles per second in the bubble-bottle (with 500ml water).
3. **Bake substrate** by ramping  $100^{\circ}\text{C}/\text{h}$  to  $1000^{\circ}\text{C}$  in tube furnace and hold for 1 h then ramp to  $25^{\circ}\text{C}$  at  $100^{\circ}\text{C}/\text{h}$

## Appendix B: The design used in the patterning process

This is the final design (Figure 5) that has been exposed, developed and etched on all the samples mentioned in the main paper.

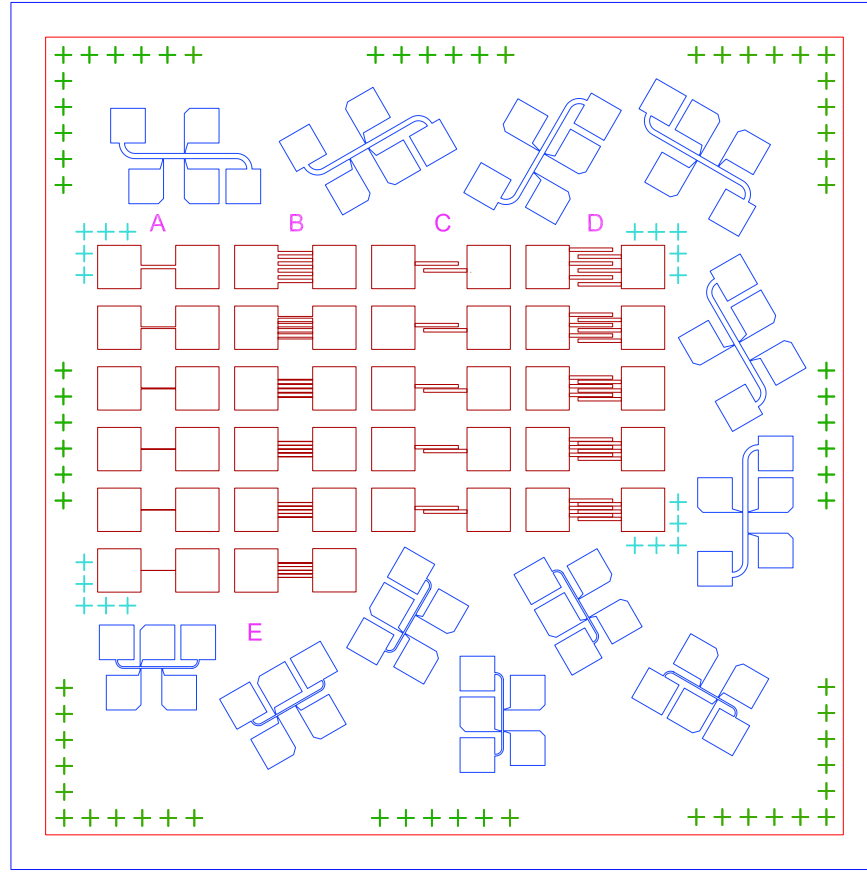


FIG. 5. The design used in the patterning process. The outer blue box is the edge of the sample. The outer red box is  $200 \mu\text{m}$  from the sample edge as a safety procedure due to consistency issues at the edge of the sample. The letters A, B, C, D and E represents different series. A and B are the same, except B has 5 times the number of channels for statistical purposes. The channel thicknesses vary from 20 to 10, 5, 2, 1 and  $0.5 \mu\text{m}$ . C and D are the same where D has 3 times the number of channels as C. Here the leakage current between neighboring channels are tested, with varying spacing in the same range as A and B. The blue units are hall bars with varying orientation and channel thicknesses. The 6 lower hall bars are in the E-series and has a channel thickness of  $10 \mu\text{m}$  and a orientation going from  $0^\circ$  to  $150^\circ$  in steps of  $30^\circ$ . The 6 upper hall bars are the same, but with a channel thickness of  $30 \mu\text{m}$ . The green and light blue marks are simply reference points used in the exposure process.

## Appendix C: Protocol for exposure, development and etching

This process should be performed in cleanroom (remember to clean every tool before using it).

### Preparing the etchant

- Prepare a **2:2:35 KI(3M):HCl(35%):H<sub>2</sub>O** by pouring 37 ml milli-Q water (or de-ionized water) H<sub>2</sub>O in a conical flask.
- Solute 0.996 g  $KI_{(s)}$  in the H<sub>2</sub>O. Use a magnetic stirrer (remember to clean the magnet) to solute the KI completely.
- When the KI is soluted, pour 2 ml 35% HCl in the solution.

### Exposure and development

The Heidelberg  $\mu$ pg 501 maskless aligner is used in this process and a manual can be found here: [http://www.nufab.northwestern.edu/files/2015/10/maskless\\_aligner\\_10222015-23ndtn9.pdf](http://www.nufab.northwestern.edu/files/2015/10/maskless_aligner_10222015-23ndtn9.pdf)

- Clean the substrate with acetone and IPA, preferably with a spray flask, then dry the substrate with N<sub>2</sub> gas. Make sure the substrate is clean by looking at it in the optical microscope. If not, clean with acetone and IPA again.
- Place the substrate on the spinner and turn on the vacuum. Close the lid and pour AZ1505 photoresist on the substrate with an micro pipette. Set the spinner to 4000 rpm for 45 seconds with a 5 seconds ramp time.
- Bake the substrate for 2 minutes at 115°C.
- Take a look in the optical microscope to see if the resist is good.
- Place the substrate in the Heidelberg  $\mu$ pg 501. Note the direction of writing if necessary. Use pneumatic focus (due to transparent sample) to locate the center of the substrate.
- Pour MF321 developer liquid in a plastic cup, and milli-Q water (or de-ionized-water) H<sub>2</sub>O in another. Immerse the substrate in MF321 for 1 minute followed by immersing directly in milli-Q water for 1 minute. Dry the substrate with N<sub>2</sub> gas.

### Wet etching

- Pour the etchant in a glass beaker, have a bottle with IPA on the side ready to spray (place some wipes on the table to soak the IPA) and pour NMP in a plastic beaker (the plastic beaker should have a lid).
- Immerse the substrate in the etchant and stir it slowly around with the tweezer for 30 seconds. Remove the substrate from the acid and spray with IPA followed by immersing in NMP. Let it be for 5 - 10 minutes at 80°C. Immerse in acetone then IPA for 1 minute each. Dry the substrate with N<sub>2</sub> gas.

### Appendix D: Results from etch testing

At first LMO was used as a hard mask and an etch-test was performed for 30s and 60s as shown in figure 6.

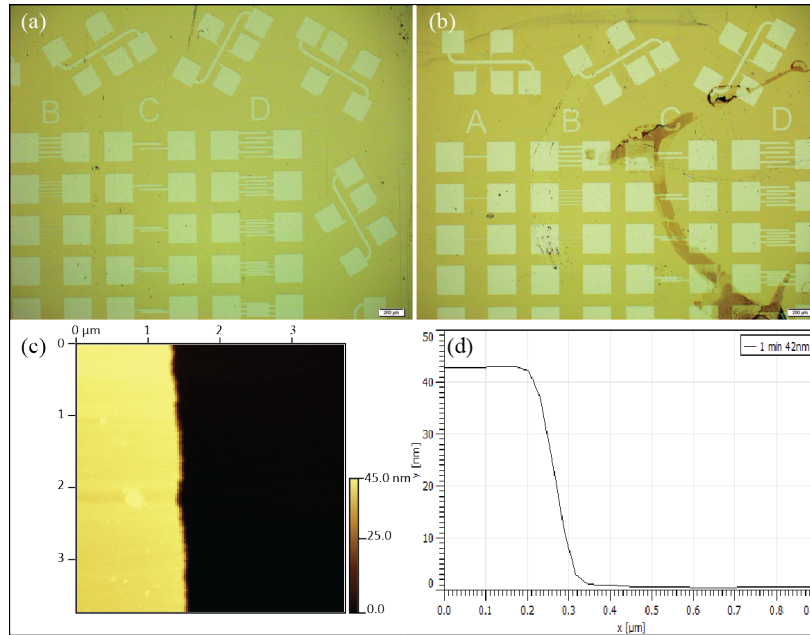


FIG. 6. LMO was used as hard mask in the beginning. An etch-test was performed with varying etch times. (a) Optical image for 30s etch time. (b) Optical image for 60s etch time. Both images show fine and well-defined structures. (c) AFM image of a channel from the 60s sample that should reveal the terrace structure of the surface, but did not. (d) Height profile of the AFM image in (c), showing that the sample was etched  $\sim 42\text{nm}$  down but did not reach the STO surface.

A test was now performed for 2,3,4 and 5 minutes to reveal the etch time necessary to reach the terrace structured surface. This is shown in figure 7.

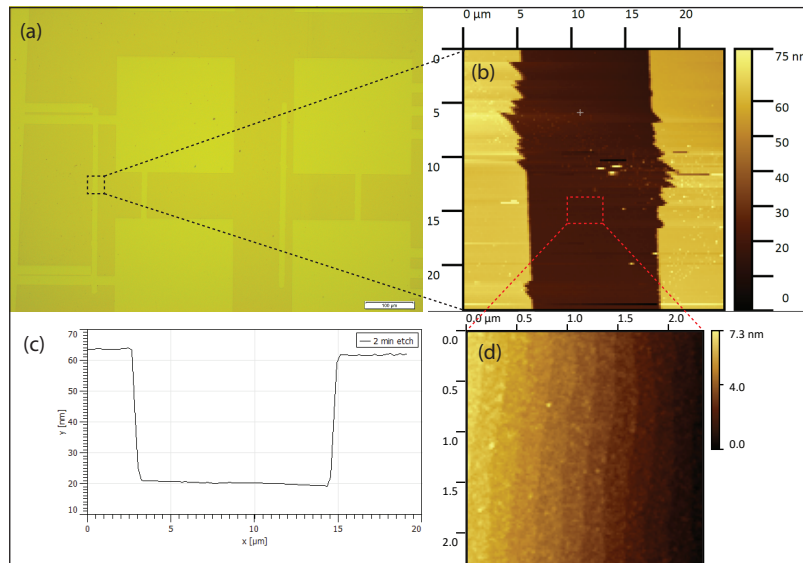


FIG. 7. 4 lines were exposed and etched for 2, 3, 4 and 5 minutes to find the best etch time. (a) Optical image of etched lines starting at 2 minutes on the left going to 5 minutes on the right. (b) AFM image (matching the black dashed box in (a)) of the 2 minutes line revealing some inconsistent etch patterns at the etches of the channel. (c) The height profile showing that the bottom should be reached ( $\sim 45\text{nm}$ ). (d) AFM image of the channel (matching the red dashed box in (b)) showing the terrace structured surface of STO.

It seems that 2 minutes etching was necessary to reach the STO surface. A sample with LSM as a hard mask was now ready to be etched with the newly discovered etch time as shown in figure 8

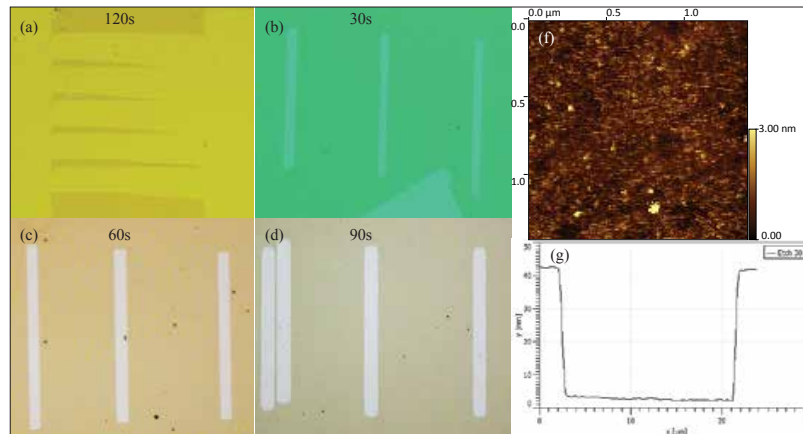


FIG. 8. First etch on a sample with LSM as a hard mask. (a) The 2 minute etch resulting in an over-etched design, meaning that 2 minutes was too long. A new etch test on LSM is therefore necessary and is shown in (b), (c) and (d) for 30s, 60s and 90s, respectively. It seems that 30s is the best, since the other are a bit too over-etched, and 30s is selected for AFM imaging. (f) AFM image of the 30s etch showing no terraces. (g) Height profile of the 30s etch.

30 seconds etch time was apparently not enough to reach the STO surfaces, however, after a meeting where it was stated that LSM and LMO are very different and only a 30s etch time is necessary, it was attempted again. This time with a new acid solution. The results were stunning! See figure 9.

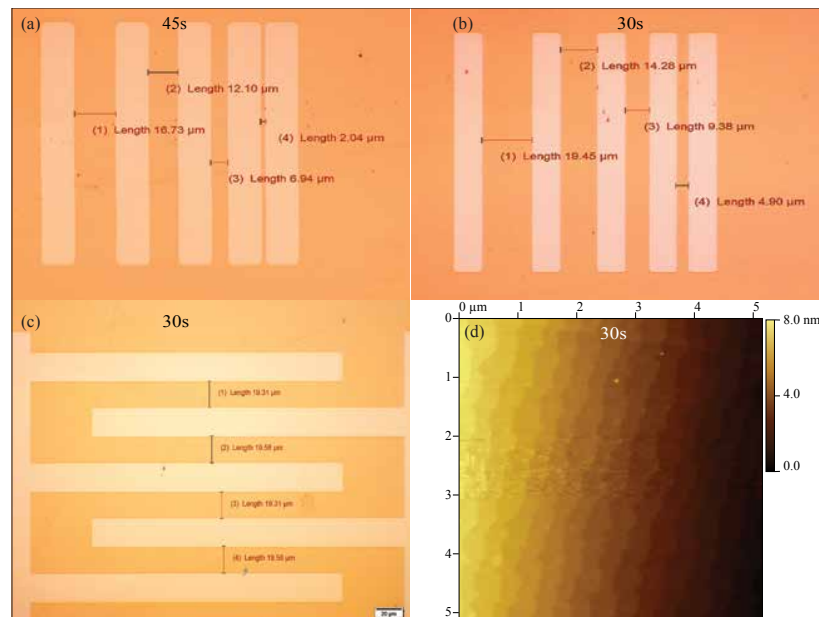


FIG. 9. Etch test with a new acid solution, for 45s and 30s. Distance between lines and channels are measured to ensure that the over-etching is as small as possible. The spacing between lines in (a) and (b) vary from 20 to 15, 10 and 5  $\mu\text{m}$ . (a) 45s etch time showing that the etch is running and it is over-etched. (b) 30s etch time showing almost no over-etching. (c) The design is etched with 30s as the etch time showing remarkable results. The spacing between neighboring channels were set to 20  $\mu\text{m}$ . (d) AFM image of the 30s etch showing clear terrace structure.

### 1. Final result of etch tests

It seems that making a new acid solution did the job. The best etch time for LSM is therefore 30s, reaching the STO surface with clear terrace structure. The over-etching is kept at a minimum (only etching  $\sim 0.5 \mu\text{m}$  out).

#### Appendix E: Etching of S2 with $W = 1\mu\text{m}$ and $W = 0.5\mu\text{m}$

As seen in figure 10, the channels with a thickness of  $1 \mu\text{m}$  has become dashed which is probably due to experimental inconsistency, since it has not been witnessed on S1 or S3. The channels with thickness  $0.5 \mu\text{m}$  is completely vanished which is consistent with the observed results from S1 and S3.

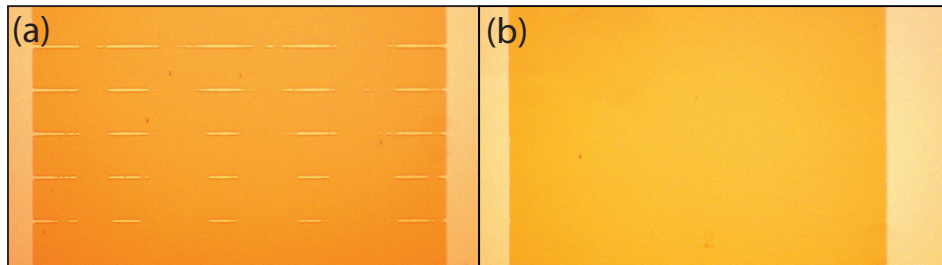


FIG. 10. Etching of (a)  $1 \mu\text{m}$  thick channels and (b)  $0.5 \mu\text{m}$  channels.

#### Appendix F: Etched channels with AFM image of channels and terraces.

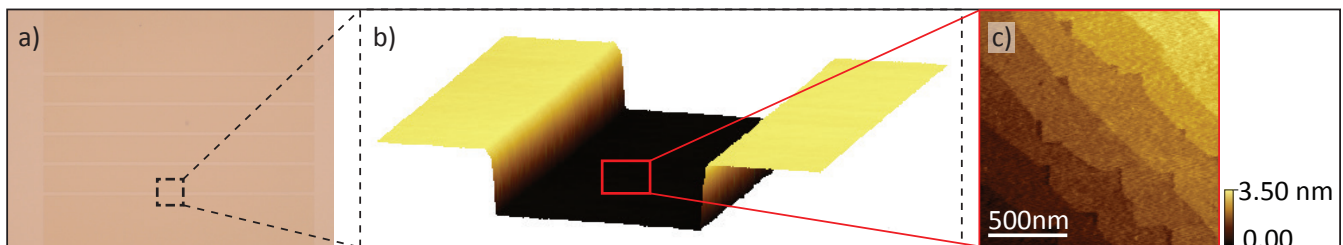


FIG. 11. Etched channels with thickness  $W = 2 \mu\text{m}$ . (a) Optical image of device. (b) 3D-rendered AFM image of black dashed square in (a). (c) AFM image of red dashed square in (b) showing terrace structure.

Appendix G: Experimental setups

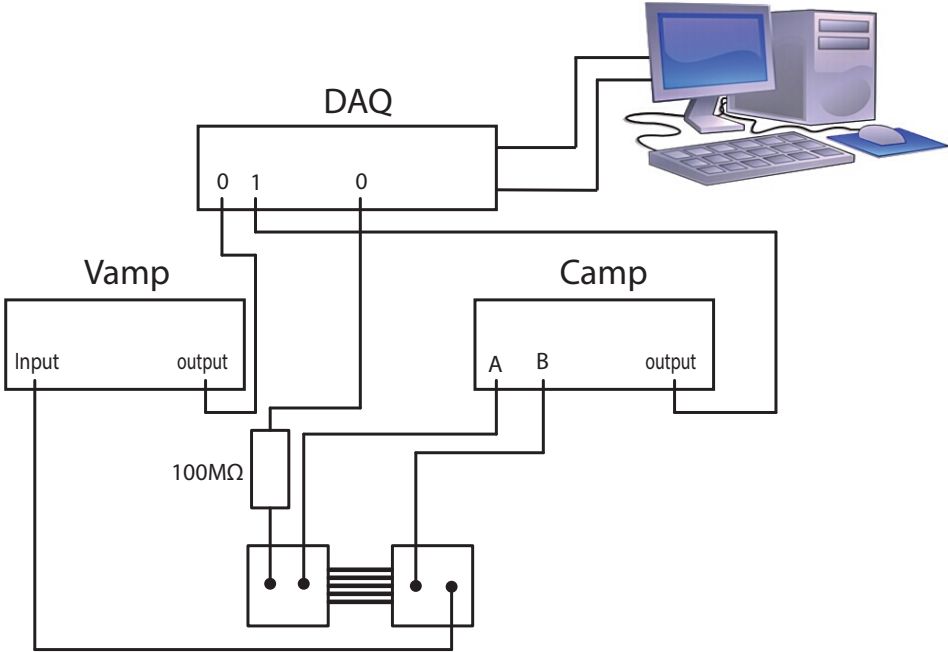


FIG. 12. The experimental setup for room temperature measurements. Breakout boxes were used to reach the bond pads, that was bonded using an ultrasonic Al-wire auto-bonder.

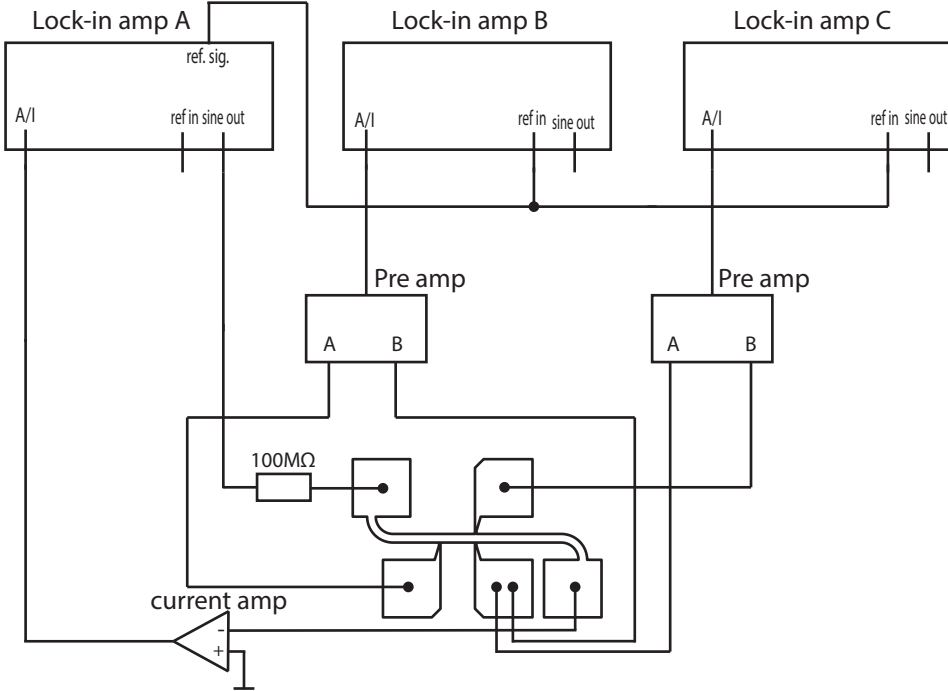


FIG. 13. The experimental setup for low temperature measurements. Breakout boxes were used to reach the bond pads, that was bonded using an ultrasonic Al-wire auto-bonder.

### Appendix H: RT measurements

Room temperature measurements were performed before loading the samples in the cryostat to ensure that the samples were functional and conducting. Figure 14 shows a table with all the measured values used in the plot in figure 2e in the main paper. All data are from 4-terminal measurements.

	Series	S1 - resist 001 (k $\Omega$ )	S2 - LSM 001 (k $\Omega$ )	S3 - LSM 111 (k $\Omega$ )
Channels	B1 - 20 $\mu\text{m}$	20780.88	18445.73	102399.01
	B2 - 10 $\mu\text{m}$	34244.04	35707.08	174006.91
	B3 - 5 $\mu\text{m}$	60454.21	64525.94	266355.92
	B4 - 2 $\mu\text{m}$	135457.22	176497.94	472410.97
	B5 - 1 $\mu\text{m}$	265407.35	BMT	673721.87
	B6 - 0.5 $\mu\text{m}$	BMT	BMT	BMT
Leakage	C1 - 20 $\mu\text{m}$	BMT	BMT	BMT
	C2 - 10 $\mu\text{m}$	BMT	BMT	BMT
	C3 - 5 $\mu\text{m}$	BMT	BMT	BMT
	C4 - 2 $\mu\text{m}$	BMT	BMT	587435.42
	C5 - 1 $\mu\text{m}$	4270479.61	92717.67	453151.1
	BMT =	Below measurement threshold		

FIG. 14. Resistance values measured (4-terminal measurements) at room temperature. BMT is short for below measurement threshold meaning that no current was measured. Note that A1, B1 and C1 is S1, S2 and S3, respectively.

Device	R ( $\Omega$ )	Orientation (deg)
HB1	137722,01	0
HB2	136641,33	30
HB3	137972,67	60
HB4	108287,9	150
HB5	107946,24	120
HB6	108370,72	90

FIG. 15. Resistance values measured for the rotating hall bars (4-point probe method) at room temperature. No clear connection between orientation and conductivity is observed.

**Appendix I: Fitting model from Fuchs et. al.**

This is the model adapted from Fuchs et. al.[17] plotted as conductance to emphasize the comparability to the cool-down data in this study.

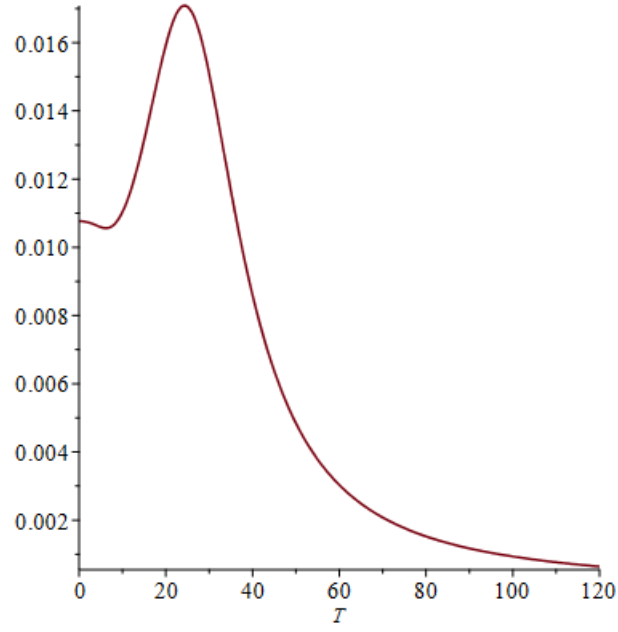


FIG. 16. Fitting model adapted from Fuchs et. al. plotted as conductance versus temperature.